Ultrasonics Sonochemistry 118 (2025) 107368

Contents lists available at ScienceDirect

Ultrasonics Sonochemistry

journal homepage: www.elsevier.com/locate/ultson

Ultrasound-responsive nanobubble-mediated sonodynamic therapy sensitizes disulfidptosis in the treatment of liver hepatocellular carcinoma☆

Yichi Chen [a,1], Xin Lin [a,1], Jiayue Qiu [b,1], Yucao Sun [a], Bolin Wu [a], Haitao Shang [a], Liwen Deng [a], Xi Wang [a], Nanxing Li [a], Chen Huang [b,*], Tianhong Zhang [c,*], Zhiguang Wu [d,*], Gang Hou [e,*], Xiaohui Yan [f], Shoufeng Wang [g], Wen Cheng [a,*]

[a] Department of Ultrasound, Harbin Medical University Cancer Hospital, Harbin 150081, China
[b] Dr. Nesher's Biophysics Laboratory for Innovative Drug Discovery, State Key Laboratory of Quality Research in Chinese Medicine & Faculty of Chinese Medicine, Macau University of Science and Technology, Taipa, Macao SAR 999078, China
[c] The First Affiliated Hospital of Harbin Medical University, Harbin 150001, China
[d] School of Medicine and Healthcare, State Key Laboratory of Robotics and System, Harbin Institute of Technology, Harbin 150080 China
[e] National Center for Respiratory Medicine, State Key Laboratory of Respiratory Health and Multimorbidity, National Clinical Research Center for Respiratory Diseases, Institute of Respiratory Medicine, Chinese Academy of Medical Sciences, Department of Pulmonary and Critical Care Medicine, Center for Respiratory Medicine, China-Japan Friendship Hospital, Beijing 100029, China
[f] State Key Laboratory of Molecular Vaccinology and Molecular Diagnostics & Center for Molecular Imaging and Translational Medicine, School of Public Health, Xiamen University, Xiamen, Fujian 361005, China
[g] Qijing Machinery Co.,Ltd, Ningbo, Zhejiang 315600, China

ARTICLE INFO

Keywords:
Hepatocellular carcinoma
Disulfidptosis
Sonodynamic therapy
Immunotherapy
Nanobubbles
RNA-seq

ABSTRACT

Disulfidptosis, a newly identified regulated cell death, is linked to tumor progression, particularly in cancers with elevated SLC7A11 expression. This study investigates SLC7A11 expression in liver hepatocellular carcinoma (LIHC) and evaluates the therapeutic potential of ICG@C3F8-KL nanobubbles (NBs) combined with sonodynamic therapy (SDT) for inducing disulfidptosis. Bioinformatics analysis of TCGA datasets revealed upregulation of SLC7A11 in LIHC tissues. The synthesized ICG@C3F8-KL NBs exhibited a mean diameter of 156.46 nm and stable properties, with high encapsulation efficiencies of 51.32 % ± 0.7 % for KL and 80.15 % ± 0.21 % for ICG. In vitro, ICG@C3F8-KL NBs, under ultrasound, generated reactive oxygen species (ROS), enhancing cytotoxicity in HepG2 cells with an IC50 lower than KL alone. These NBs also inhibited cell migration and colony formation, suggesting disulfidptosis induction via altered glucose uptake and NADP+/NADPH ratio, as well as F-actin contraction. In vivo, ICG@C3F8-KL NBs accumulated in tumor tissues and suppressed growth without significant toxicity. Unsupervised clustering of disulfidptosis-related genes in TCGA LIHC cohort identified subtypes with distinct prognoses, and a predictive model based on five key genes was developed. In conclusion, ICG@C3F8-KL NBs, combined with ultrasound, effectively induce disulfidptosis, offering a promising strategy for LIHC treatment, with the potential for personalized therapy informed by disulfide-associated gene signatures.

1. Introduction

Disulfidptosis is a recently identified kind of programmed cell death triggered by an accumulation of excess cystine, causing disulfide stress. [1–3] The main features of disulfidemia include F-actin contraction, accumulation of disulfides (e.g., cystine), and NADPH depletion, especially when glucose uptake is suppressed in vitro [1,4,5]. Disulfidptosis is more likely to occur in tumor cells, which typically have a higher

Abbreviations: TME, tumor microenvironment; LIHC, liver hepatocellular carcinoma; NBs, nanobubbles; UTMD, ultrasound-targeted microbubble destruction; US, ultrasound; ROS, reactive oxygen species.

☆ This article is part of a special issue entitled: 'Biomaterial Assembly and Theranostics' published in Ultrasonics Sonochemistry.

* Corresponding authors.
E-mail addresses: chuang@must.edu.mo (C. Huang), zth3856@126.com (T. Zhang), zhiguangwu@hit.edu.cn (Z. Wu), hougangcmu@163.com (G. Hou), chengwen@hrbmu.edu.cn (W. Cheng).

[1] These authors contributed equally to this work.

https://doi.org/10.1016/j.ultsonch.2025.107368
Received 7 March 2025; Received in revised form 13 April 2025; Accepted 21 April 2025
Available online 23 April 2025

metabolic rate, than in apoptosis or other forms of necrotic cell death [1,6,7]. Additionally, studies have confirmed that disulfidptosis may be harnessed to specifically target and eradicate tumor cells, thereby enhancing systemic antitumor immunity, reducing immunosuppressive effects in the tumor microenvironment, and increasing antitumor efficacy [8]. Intriguingly, LIHC is often considered a highly energy-demanding and metabolically active tumor, [9] and several studies suggest that limiting glucose intake is an effective strategy for its therapy [10–12]. However, the application of disulfidptosis in LIHC has yet to be investigated. Therefore, the development of therapeutics that elicit disulfidptosis is of great potential for the treatment of LIHC.

However, despite the promising therapeutic potential of disulfidptosis inducers, their development still presents challenges in clinical translation [13]. One significant hurdle is the low solubility of disulfidptosis inducers, like KL-11743 (KL), which reduces their bioavailability and in vivo delivery effectiveness [14]. Nanotechnology-based methods have presented promise in overcoming these obstacles and improving the therapeutic potential of disulfidptosis. These approaches are designed to enhance the solubility of disulfidptosis inducers, thereby overcoming the limitations associated with their poor solubility and improving their intracellular delivery.[15,16].

Furthermore, during disulfidptosis, excessive ROS-induced lipid peroxidation (LPO) accumulation in cells is recognized as a marker of NADPH depletion, with cystine buildup being the primary contributing factor. Therefore, effective strategies to elevate ROS levels in cancer cells can promote disulfidptosis in tumor cells more effectively. Sonodynamic therapy (SDT), triggered by ultrasound radiation, has attracted significant attention because of its non-invasive approach, ability to penetrate deep tissues, and precise targeting potential [17,18]. Recent evidence suggests that SDT induces ROS generation, which can disrupt cellular redox equilibrium, particularly the NADP+/NADPH ratio [19]. In this study, we developed and synthesized an ultrasound-activated nanomedicine (ICG@C3F8-KL NBs) (Fig. 1), which not only suppressed the growth of the primary tumor but also stimulated the systemic immune response. Significantly, ICG@C3F8-KL NBs could efficiently produce ROS when exposed to ultrasound radiation, resulting in the decomposition of ICG@C3F8-KL NBs and consequent release of KL. Cysteine accumulation and disulfidptosis were caused by the released KL suppression of Glut1 in tumor cells, which decreased the pentose phosphate pathway and glucose transport. Meanwhile, the ROS

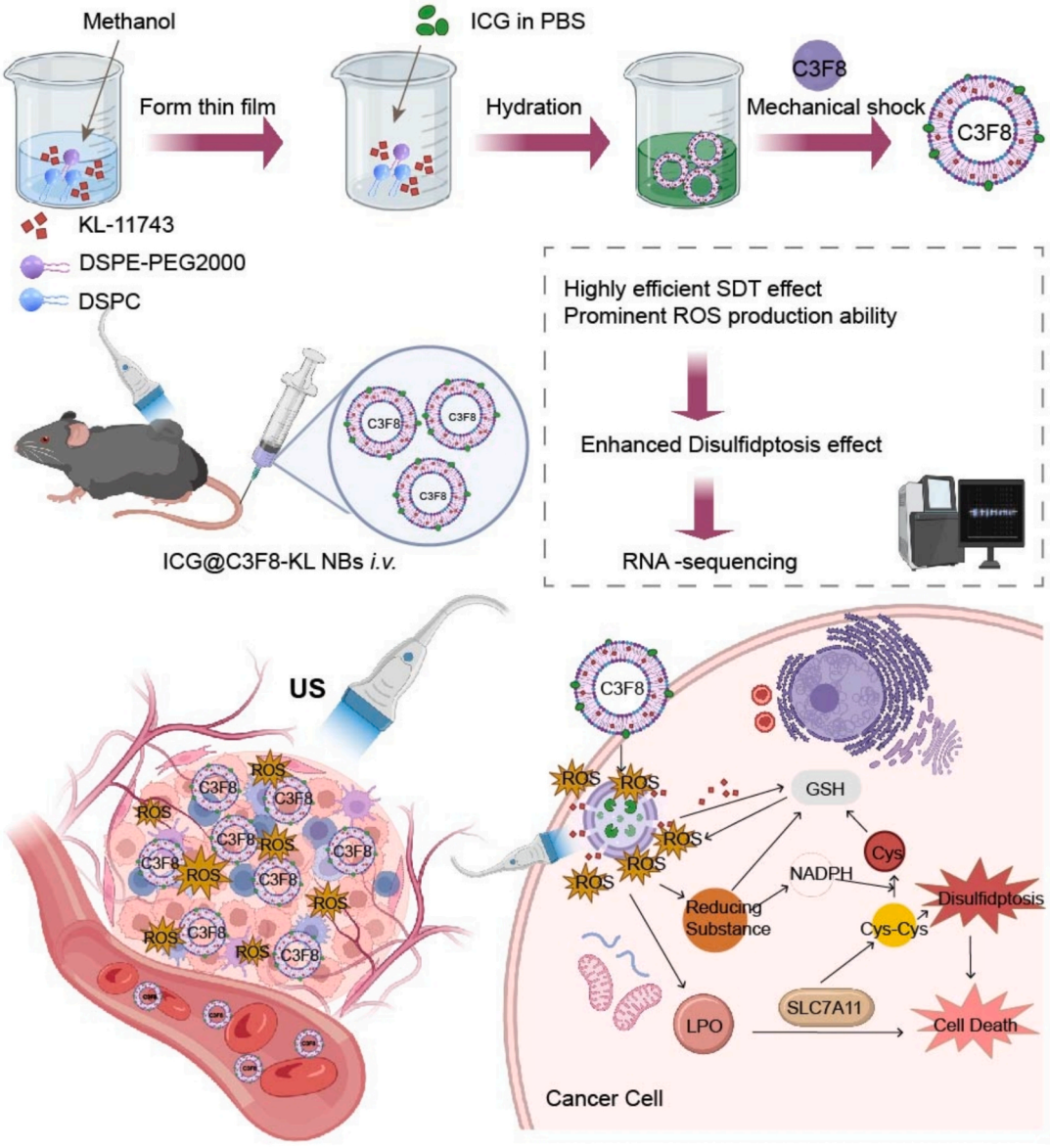

Fig. 1. Schematic diagram of the assembly process of ICG@C3F8-KL NBs and mechanism of mediating SDT-sensitizing disulfidptosis in treating LIHC.

produced by ultrasound could synergistically disrupt the intracellular redox balance, promoting disulfidptosis. The mechanism underlying the synergy between disulfidptosis and SDT was explored through RNA-Seq, further highlighting the clinical potential of combining disulfidptosis with SDT for the treatment of liver hepatocellular carcinoma (LIHC).

2. Results and discussion

2.1. Expression of SLC7A11 in LIHC

It has been demonstrated that tumors with elevated expression of SLC7A11 are more likely to induce disulfidptosis. To investigate the expression of SLC7A11 in LIHC, we first used bioinformatics techniques to examine the cancer genome atlas (TCGA) datasets, which comprise 369 instances of LIHC and 160 normal cases. According to the research, LIHC tissues had higher levels of SLC7A11 than nearby normal tissues (Fig. S1). To validate the elevated levels of SLC7A11 observed in LIHC tissues through bioinformatics analysis, we performed Western blot analysis to assess SLC7A11 expression in HepG2 and Hepa1-6/luc cells. As shown in Fig. S2, both HepG2 and Hepa1-6/luc cells exhibited significantly higher expression levels of SLC7A11 compared to normal controls, consistent with the bioinformatics results. Quantification of the Western blot bands further confirmed the upregulation of SLC7A11 in these cell lines. These findings provide direct evidence supporting the elevated expression of SLC7A11 in liver cancer cells, reinforcing its potential role in the progression of disulfidptosis.

2.2. Synthesis and characterization of ICG@C3F8-KL NBs

The preparation of ICG@C3F8-KL NBs was carried out with rotary evaporation phacoemulsification. As shown in the Fig. 1, first, the selected phospholipids (DSPC, DSPE-PEG2000) are dissolved in an organic solvent (dichloromethane/methanol mixture), and KL-11743 was added at the same time to form a uniform mixed solution. Subsequently, the organic solvent is removed by rotary evaporation to form a uniform phospholipid-drug mixed film in the flask, and ICG in PBS was added for hydration to allow the phospholipids to spontaneously form vesicles. Then, in an inert gas (perfluoropropane) environment, mechanical oscillation is used to induce bubble core formation, further enhancing the ultrasound imaging performance and stability of the microbubbles. Subsequently, the unencapsulated KL-11743 and ICG are removed by low-speed centrifugation to obtain stable ultrasound microbubbles, and morphology is observed by transmission electron microscopy (TEM) and Scanning Electron Microscopy (SEM). Based on TEM and SEM images, the resulting revealed that the ICG@C3F8-KL NBs exhibited a uniform spherical morphology with a smooth surface, consistent with their nanoscale structure (Fig. 2a, Fig. S3a). (Reviewer 2 Comment 4) In addition, we detected the UV–vis spectra of all components that were involved in the preparation of the synthesized ICG@C3F8-KL NB. From the UV spectra of KL and ICG, we observed that KL exhibits a characteristic absorption peak around 247 nm, while ICG has two apparent absorption peaks at 715 nm and 780 nm. As shown in Fig. 2b and Fig. S3b, the UV spectrum of ICG@C3F8-KL NBs displays three characteristic peaks at approximately 247 nm, 715 nm, and 780 nm, which proves the successful integration of ICG and KL. The KL loading in ICG@C3F8-KL NBs was calculated to be 5.78 % ± 0.8 % (w/w), and the encapsulation efficiency (EE) was 51.32 % ± 0.7 %. Similarly, the ICG had a drug loading of 10.20 % ± 0.01 % (w/w), with an EE of 80.15 % ± 0.21 %.

Furthermore, Fourier-transform infrared spectroscopy (FT–IR) was conducted to investigate the chemical composition and molecular interactions. The successful incorporation of ICG and KL-11743 into NBs was confirmed by infrared (IR) spectroscopy based on the following spectral characteristics: retention and superposition of characteristic peaks—the distinct absorption band of ICG at 1525 cm^{-1} (aromatic ring) and KL-11743 at 1728 cm^{-1} (C=O stretching) were observed at 1525 cm^{-1} and 1664 cm^{-1}, respectively, after loading. The slight shift of the C=O peak suggests a possible alteration of the local microenvironment, while the preservation of these signals indicates that both agents remained chemically intact within the liposomal complex. Furthermore, the characteristic CH_2 stretching vibration of lipids at 2974 cm^{-1} and the phosphate ester peak shifting from 1110 to 1101 cm^{-1} were

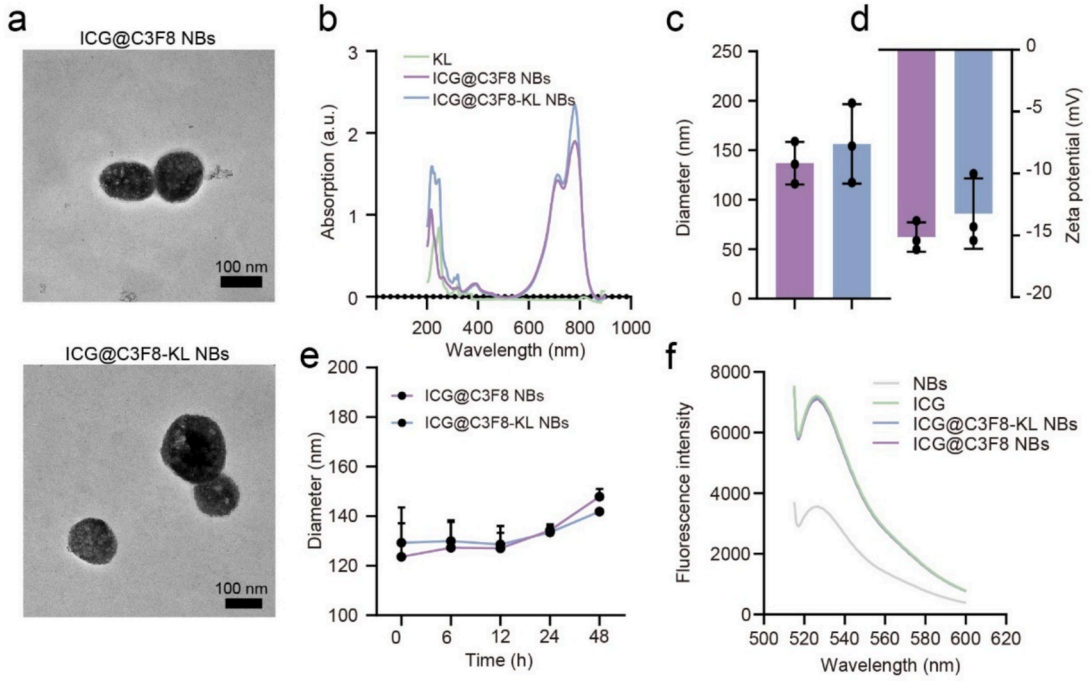

Fig. 2. Characterization of ICG@C3F8-KL NBs. (a) TEM image of ICG@C3F8-KL NBs. Scale bar: 120 nm, 150 nm. (b) The UV–Vis absorption spectra of KL, ICG@C3F8 NBs, and ICG@C3F8-KL NBs. (c) The hydrodynamic diameter of ICG@C3F8-KL NBs. (d) The zeta potential of ICG@C3F8-KL NBs. (e) The hydrodynamic diameter of ICG@C3F8-KL NBs in 48 h. (f) The SOSG fluorescence spectra of ICG@C3F8 NBs and ICG@C3F8-KL NBs upon ultrasound irradiation.

retained, although with changes in intensity, implying that drug encapsulation may alter lipid packing and membrane organization. Emergence of new interaction-associated peaks was also observed: the appearance of a peak at 1566 cm^{-1} is likely attributed to hydrogen bonding interactions (e.g., between the C=O group of KL-11743 and the O–H group of phospholipid headgroups) or π–π stacking between the aromatic rings of ICG and the hydrophobic lipid tails. Additionally, the band at 1220 cm^{-1} may correspond to interactions between the C–O–C groups of the drug molecules and the phosphate moieties of the lipids. Peak shifts and intensity variations provided further evidence of molecular interactions: the O–H stretching band of liposomes exhibited a blue shift from 3450 to 3423 cm^{-1}, suggesting the formation of a strengthened hydrogen bonding network upon drug encapsulation. A slight shift in the N–H/O–H vibration band of ICG from 3876 to 3884 cm^{-1} further reflects the altered microenvironment surrounding the amino/hydroxyl functionalities post-encapsulation. Collectively, these IR spectral changes indicate that ICG and KL-11743 were successfully encapsulated within NBs via non-covalent interactions, such as hydrophobic interactions and hydrogen bonding, without chemical bond cleavage, and that the overall structural integrity of the NBs carrier was maintained. (Fig. S3c).

The in vitro drug release profiles of ICG and KL from ICG@C3F8-KL NBs were studied at different times to evaluate the effect of ultrasound (US) stimulation on drug release. Regarding the selection of ultrasound (US) parameters (1.0 W/cm^2, 50 % duty cycle, 30 s, 1 MHz), we based our choices on previous studies, preliminary optimization experiments, and safety considerations. Specifically: 1.0 W/cm^2: This intensity was chosen to balance therapeutic efficacy and avoid excessive tissue heating or cavitation-induced damage [20]. 50 % duty cycle: This setting optimizes ultrasound exposure while minimizing unnecessary energy deposition, reducing potential thermal effects. 30 s duration: Based on preliminary tests, this duration was found to be sufficient for effective activation without inducing significant off-target effects [1]. 1 MHz frequency: This frequency is commonly used in therapeutic ultrasound due to its optimal tissue penetration and controlled cavitation effects [6]. These parameters were systematically optimized to ensure efficient activation of the nanobubbles, effective singlet oxygen generation, and minimal toxicity.

As shown in Fig. S4, under normal physiological conditions (PBS, pH 7.4), both ICG and KL were continuously released within 72 h, and the release rate was significantly higher under ultrasound exposure. Under ultrasound stimulation (1.0 W/cm^2, 1 MHz, 50 % duty cycle, 30 s), the release rate was significantly accelerated, with 93 % of ICG and 89 % of KL released within 72 h, indicating that ultrasound significantly enhanced drug release from nanobubbles.

Measurements by dynamic light scattering (DLS) indicated that the mean hydrodynamic diameter of the ICG@C3F8-KL NBs was 156.46 nm ± 40.09 nm (Fig. 2c and d), and the surface zeta potential was about −13.25 mV ± 2.85 mV. ICG@C3F8-KL We also conducted additional experiments to assess the stability of NBs in both water and cell culture medium over seven days. As shown in the Fig. 2e and Fig. S5, the results demonstrated that the nanobubbles maintained their structural integrity and exhibited minimal size variation (<10 %) in both conditions, indicating favorable stability.

KL and ICG are drugs with low bioavailability. However, the ICG@C3F8-KL NBs exhibit good encapsulation efficiency for both ICG and KL. Due to their nanoscale size, they can significantly penetrate tumors via the enhanced permeability and retention (EPR) effect [21–23]. We conducted studies utilizing the SOSG probe to verify the synthesized NBs' capacity to generate ROS [24]. The formation of SOSG endoperoxide (SOSG-EP) when monoclinic oxygen ($^1O_2$) reacts with SOSG prevents the transfer of internal electrons, leading to an increase in fluorescence at the excitation/emission wavelengths of 504/525 nm [25]. As depicted in Fig. 2f, SOSG fluorescence intensity enhanced after ultrasound irradiation of ICG and ICG@C3F8-KL NBs. These results confirm that because ICG can produce ROS, sonodynamic treatment can be much more effective by ICG@C3F8-KL NBs.

Besides, NBs can enhance bioavailability, permeability, and solubility.[26] The above findings indicate that we successfully produced ICG@C3F8-KL NBs capable of producing ROS. Thus, it has the potential to serve as a sonosensitizer, enhancing the effectiveness of SDT, and can be utilized in the treatment of cancer, thereby increasing the efficiency of treatment and minimizing side effects.

2.3. ROS generation and cytotoxic effects of ICG@C3F8-KL NBs under ultrasound exposure in vitro

First, we aimed to evaluate the impact of different drug administration ratios on treatment outcomes, testing various combinations of ICG and KL at mass ratios of 1:1, 2:1, 1:2, 3:1, and 1:3, while maintaining constant total drug loading and NBs concentration across all groups. The CCK-8 assay was employed to assess cell viability after 24 h of treatment. The results indicated that all tested drug combinations inhibited cell growth to varying extents, with the 1:1 ratios demonstrating the most significant inhibition of cell viability. Interestingly, these two ratios, where the doses of ICG and KL were more balanced, provided better therapeutic outcomes than the others. Therefore, we chose this ratio to make NBs in subsequent experiments (Fig. S6).

For a visual evaluation of the ability of ICG@C3F8-KL NBs to produce ROS under ultrasound exposure, HepG2 cells treated with different conditions were stained with the 2′,7′-dichlorodihydrofluorescein diacetate (DCFH-DA) probe (green) and then observed under a fluorescence microscope. According to the findings, HepG2 cells with ICG@C3F8-KL NBs treatment under ultrasonic radiation exhibited a much greater green fluorescence than cells treated with other substances (Fig. 3a, Fig. S7). To further assess the impact of increased ROS levels on mitochondrial function, we performed JC-1 staining to evaluate mitochondrial membrane potential (ΔΨm). As shown in Fig. S8, cells in the NC and ICG@C3F8-KL NBs group exhibited strong red fluorescence, indicating intact mitochondrial membrane potential. In contrast, ICG@C3F8-KL NBs + US treated cells displayed a significant shift from red to green fluorescence, suggesting mitochondrial depolarization, indicating mitochondrial dysfunction induced by increased ROS levels. These results provide additional evidence that ROS generation disrupts mitochondrial integrity, further contributing to the therapeutic effects observed.

To investigate the anticancer roles of ICG@C3F8-KL NBs in vitro, cytotoxicity of ICG@C3F8 NBs under ultrasound irradiation, ICG@C3F8-KL NBs under ultrasound irradiation, and KL was first evaluated using the cell counting kit-8 (CCK-8) assay. The half-inhibitory concentration (IC50) of ICG@C3F8-KL NBs on HepG2 cells under ultrasound irradiation was 67.72 ± 1.1 μM, nearly half of KL (IC50 = 93.07 ± 2.6 μM) and one-sixth of ICG@C3F8 NBs under ultrasound irradiation (IC50 = 410.2 ± 0.5 μM), indicating that ICG@C3F8-KL NBs are highly cell-killing under ultrasonic irradiation (Fig. 3b).

Furthermore, to further demonstrate the anticancer activity of ICG@C3F8-KL NB in vitro under ultrasound exposure, live/dead assays were performed. Treatment of HepG2 cells with ICG@C3F8 NBs + US (SDT), ICG@C3F8-KL NBs, PBS (NC), ICG@C3F8-KL NBs + US (SDT + KL) along with KL, and later staining with PI (red) and Calcein-AM (green). The findings of fluorescence microscopy exhibited that HepG2 cells with SDT + KL treatment were primarily dead (red), underscoring the crucial anticancer impact of ICG@C3F8-KL NBs in vitro when exposed to ultrasound (Fig. 3c).

Subsequently, a colony formation test was applied to evaluate the proliferation of HepG2 cells under various treatments visually. The findings exhibited that PBS-treated HepG2 cells produced closely spaced colonies within the field of vision. HepG2 cells treated with KL formed fewer colonies, and those treated with ICG@C3F8-KL NBs showed a significant decrease in colony formation under ultrasound radiation, indicating that SDT + KL notably inhibits colony formation in HepG2 cells (Fig. 3d, Fig. S9).

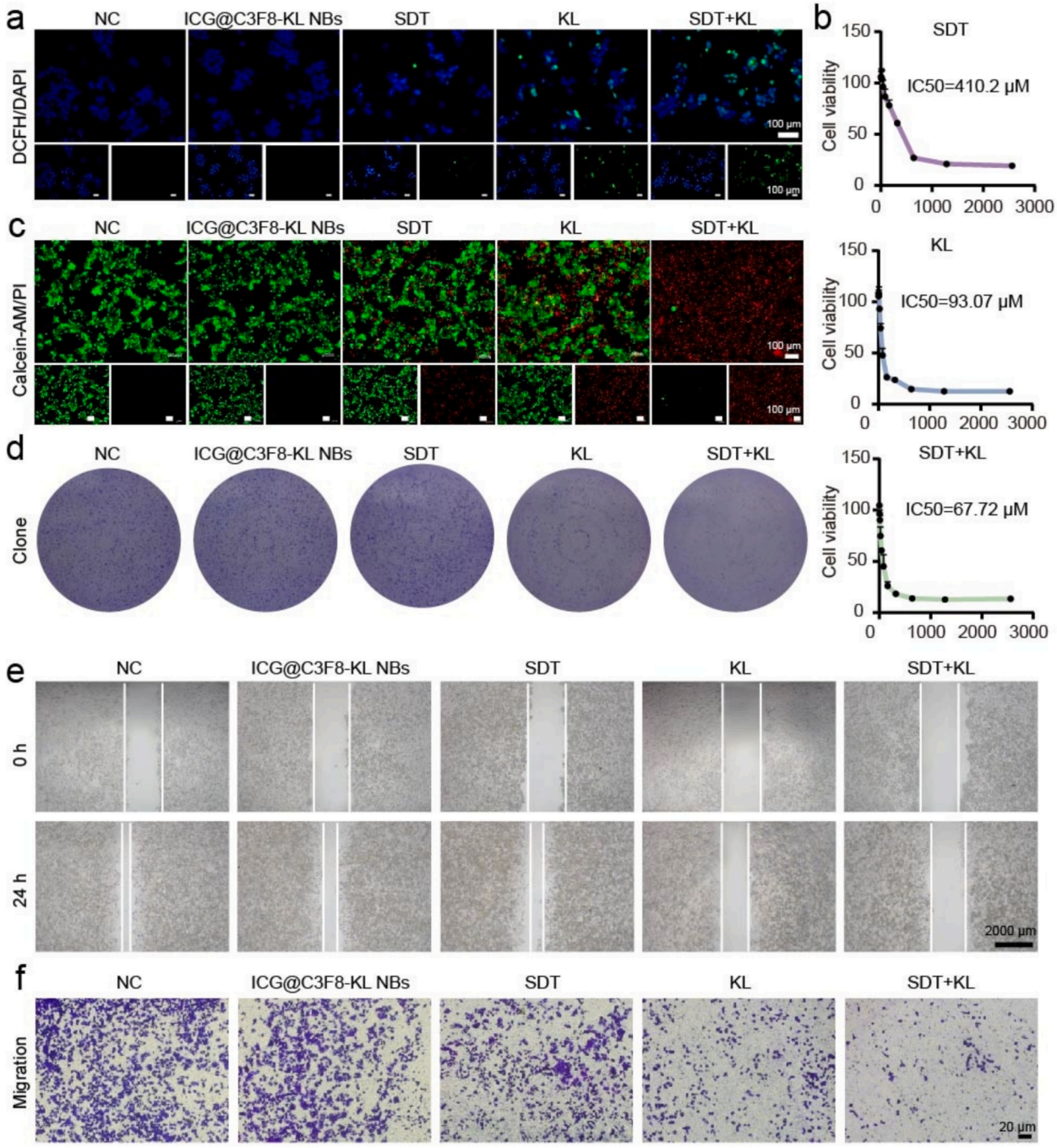

Fig. 3. ROS production and cytotoxicity with ICG@C3F8-KL NBs under ultrasound radiation. (a) Representative fluorescence images showing ROS production in HepG2 cells after different treatments. Scale bar = 100 μm. (b) In vitro cytotoxicity of different treatments on HepG2 cells for 24 h, n = 3. (c) Cell viability and death were assessed using live/dead staining after different treatments. Scale bar = 100 μm. (d) Colony formation assay under different treatments. (e) Wound healing assay to assess cell migration in HepG2 cells under different treatments. Scale bar = 2000 μm. (f) Transwell assay to evaluate cell migration in HepG2 cells under different treatments. Scale bar = 20 μm.

Previous studies have indicated that ROS can effectively inhibit tumor cells' metastasis [27,28]. A wound-healing assay was performed to evaluate the impact of ICG@C3F8-KL NBs on tumor cells. The results demonstrated that SDT + KL could markedly suppress wound closure, suggesting its potential to inhibit the migration of tumor cells (Fig. 3e, Fig. S10). A transwell experiment was performed to explore the anti-metastatic properties of ICG@C3F8-KL NBs further. The findings displayed that SDT + KL successfully prevented the metastasis of tumor cells by dramatically reducing tumor cell motility. (Fig. 3f, Fig. S11) These results reveal that, when exposed to ultrasound, ICG@C3F8-KL NBs can efficiently target malignancies and prevent the metastases of tumor cells.

2.4. ICG@C3F8-KL NBs triggered disulfidptosis under ultrasound exposure

Studies have demonstrated that in glucose-deprived conditions, tumors with high SLC7A11 expression, such as LIHC, [28–30], consume significant amounts of NADPH, [31,32] which leads to cystine accumulation and cell skeleton contraction, triggering a distinct cell death

mechanism called disulfidptosis. Furthermore, studies have suggested that when levels of ROS are elevated in the cell, the NADP+/NADPH system is a critical regulator, and sensitizers can produce substantial ROS under low-intensity ultrasound radiation [22,33]. Thus, it can be inferred that under ultrasonic radiation, ICG@C3F8-KL NBs release ROS, which facilitates the consumption of NADPH in cells, mainly when glucose levels are low. Cysteine external accumulation accelerates NADPH depletion, which causes tumor cells to undergo disulfidptosis and slows tumor development.

To prove that cell death is due to sonodynamics, we improved the tumor cell sensitivity to KL drugs. First, it was assessed how ICG@C3F8-KL NBs inhibited tumor cells' glucose absorption when exposed to ultrasonic radiation. To assess this, glucose levels in HepG2 cells treated with various therapies were measured using a glucose uptake assay kit. According to the results, SDT + KL was able to successfully decrease glucose absorption because its cellular glucose uptake under ultrasonic radiation was 3633.6 ± 120.1 μg/mg, which was 67.9 % and 53.2 % of KL (5351.4 ± 523.7 μg/mg) and SDT (6834.3 ± 139.2 μg/mg), separately (Fig. 4a). Immunofluorescence staining was conducted on cells undergoing various treatments to investigate the alterations in F-actin in HepG2 cells. According to the findings, the F-actin contraction (green) in the SDT + KL group was considerably higher than that of the SDT and KL

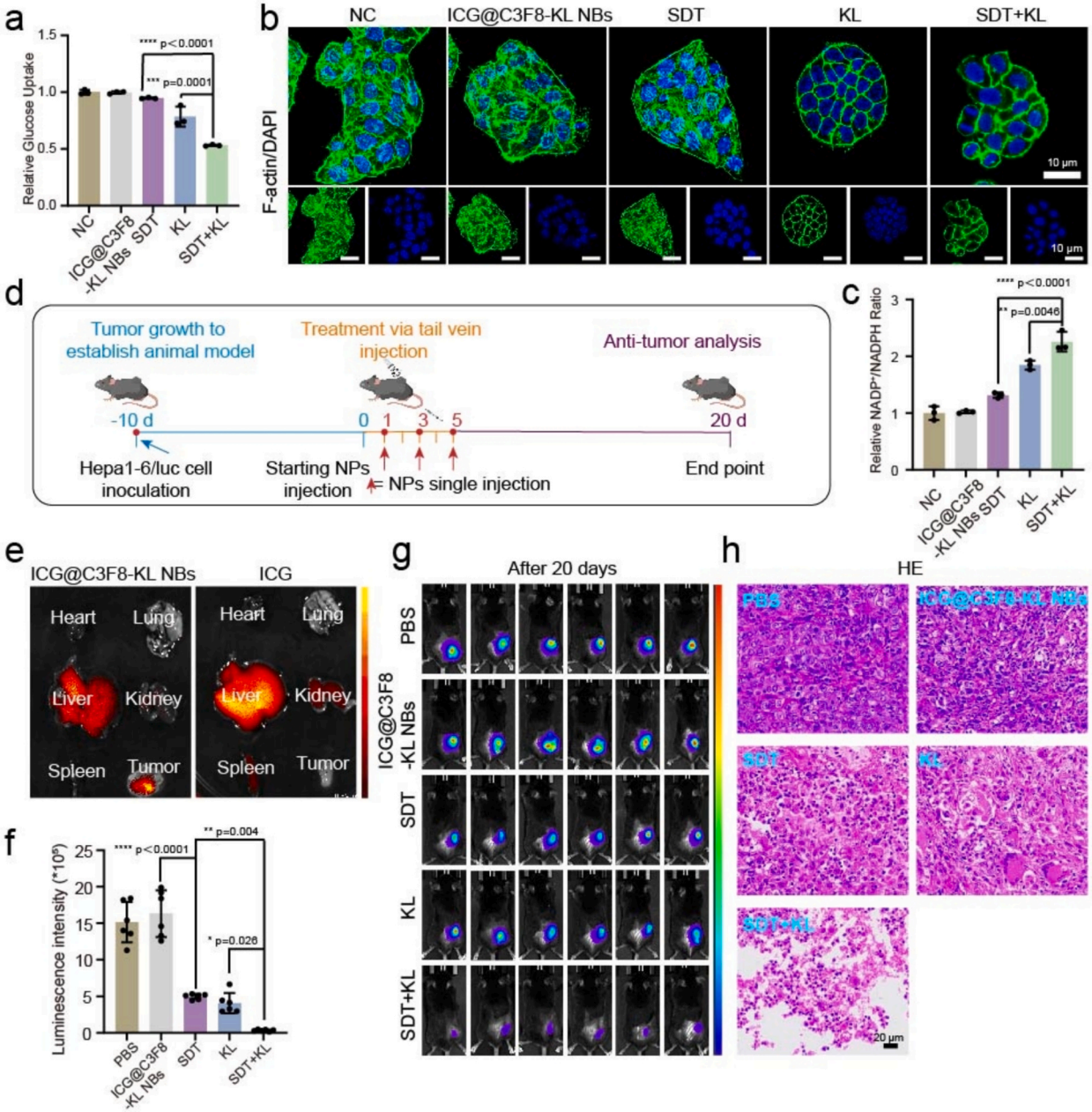

Fig. 4. ICG@C3F8-KL NBs promote disulfidptosis in vitro and in vivo under ultrasound exposure. (a) The glucose uptake in HepG2 cells was quantitatively assessed following treatments, n = 3. Data are presented as mean ± SD. Statistical significance was calculated by one-way ANOVA, ****p < 0.0001, ***p < 0.001. (b) Representative CLSM images showing alterations in F-actin within HepG2 cells after different treatments. Scale bar = 10 μm. (c) The quantitative analysis of NADP+/NADPH levels in HepG2 cells following different treatments, n = 3. Data are presented as mean ± SD. Statistical significance was calculated by one-way ANOVA, ****p < 0.0001, **p < 0.01. (d) Schematic illustration of treatment schedule. (e) Fluorescence images of primary organs and tumors at 48 h. (f) Luminescence intensity of tumor sites at day 20 are presented as mean ± SD. Statistical significance was calculated by one-way ANOVA, ****p < 0.0001, **p < 0.01, *p < 0.05. (g) Bioluminescence images of tumor-bearing mice from different groups on the 20th day of the follow-up period. (h) H&E staining of tumor tissues after different treatments. Scale bar = 100 μm.

groups (Fig. 4b). Lastly, the intracellular NADP+/NADPH ratios of HepG2 cells that were treated under various conditions were determined with the use of a NADP+/NADPH assay kit. The findings revealed that under ultrasound radiation, the intracellular NADP+/NADPH ratio elevated to 2.25 ± 0.17 in the SDT + KL group, which was 1.2 and 1.7 times higher than that in the KL group (1.84 ± 0.07) and the SDT group (1.31 ± 0.05), separately. These findings indicate that under ultrasound radiation, SDT + KL significantly enhances intracellular NADPH depletion compared to KL alone (Fig. 4c).

To further confirm the occurrence of disulfidptosis in our experimental model, we examined the expression levels of key cytoskeletal-associated proteins, FLNA, TLN1, and MYH9, by Western blot analysis. As shown in Fig. S12, treatment with SDT + KL treatment led to a significant downregulation of FLNA and TLN1, while MYH9 expression was markedly increased. These alterations are consistent with the characteristic cytoskeletal collapse associated with disulfidptosis [6,34]. Furthermore, pretreatment with dithiothreitol (DTT), a disulfidptosis inhibitor, effectively rescued the expression levels of these proteins, indicating that their dysregulation was specifically linked to disulfidptosis rather than nonspecific cellular stress responses. These findings provide strong molecular evidence supporting the involvement of disulfidptosis in our system.

2.5. Antitumor efficacy of ICG@C3F8-KL NBs under ultrasound radiation

Following the in vitro anticancer evaluation of ICG@C3F8-KL NBs, its antitumor activity in vivo was also assessed (Fig. 4d). The biodistribution of ICG@C3F8-KL NBs in mice with tumors was initially examined. Subcutaneous tumor models of Hepa1-6/luc LIHC were established in 6-week-old healthy C57BL/6 mice. 48 h after the drug was administered, ex vivo imaging of the tumor tissues and organs was carried out. The tumor displayed the maximum fluorescence intensity, evidently surpassing that of other organs (Fig. 4e).

The in vivo antitumor efficacy of ICG@C3F8-KL NBs combined with ultrasound (US) exposure was evaluated in C57BL/6J mice bearing subcutaneous Hepa1-6/luc tumors. Regarding anticancer effectiveness, the findings presented that the impact of ICG@C3F8-KL NBs alone was not satisfactory, and there was no evident variation in tumor inhibition in contrast to PBS. With a tumor inhibition rate of 97.8 ± 0.01 %, SDT + KL exhibited the strongest tumor inhibition efficacy, while KL and SDT had tumor inhibition rates of 72.51 ± 0.11 % and 66.64 ± 0.04 %, respectively (Fig. 4f–g, Fig. S13a). At the end of the treatment period (20 days), tumor masses in the combination treatment group were notably smaller, with a significant reduction compared to the control and other treatment groups, further supporting the antitumor potential of this approach (Fig. S13b).

To verify the anticancer impact of SDT + KL, tumor tissues were stained with hematoxylin and eosin (H&E) and TUNEL staining. The findings demonstrated that compared to tumor tissues from other treatment groups, those from SDT + KL-treated mice exhibited a large drop in cell count and a significant decrease in density (Fig. 4h, Fig. S14a).

Additionally, Ki-67 immunofluorescence staining showed a marked decrease in proliferating cells in the combination treatment group, suggesting that SDT + KL effectively inhibited tumor cell proliferation. These findings are consistent with SDT enhances the therapeutic effects of KL, not only by promoting drug release but also by inducing apoptosis and suppressing cell proliferation within the tumor (Fig. S14b).

Regarding safety, the findings showed that 20 days after treatment, there was no apparent decrease in body weight in SDT + KL-treated mice compared to those treated with PBS, suggesting that ICG@C3F8-KL NBs exhibit favorable biocompatibility and biosafety under ultrasound exposure (Fig. S15). Additionally, we conducted liver and kidney function tests, including serum ALT, AST, BUN, and CRE levels. As shown in Fig. S16, no significant abnormalities were observed in these biochemical markers, suggesting that our treatment strategy does not cause apparent systemic toxicity. These findings support the good biocompatibility and potential clinical applicability of our NBs.

2.6. Identification of disulfidptosis subtypes in the TCGA cohort

In this study, differential expression of mRNA and lncRNA transcripts (counts) was estimated using the edgeR R package, with thresholds set at $|\log2FC| > 1$ and p.adjust < 0.05. The NC1 and SDT + KL1 groups were found to have 1,077 differentially expressed genes, of which 779 were upregulated and 298 downregulated, according to the data (Fig. 5a).1225 differential genes were identified in the SDT + KL2 and NC2 groups, including 875 up-regulated genes and 350 down-regulated genes (Fig. 5b). KEGG enrichment analysis was performed using the two groups of differential genes, the results showed that complement and coagulation cascades, insulin secretion, and cytokine-cytokine receptor interaction were significantly enriched in SDT + KL1 vs. NC1, suggesting that disulfidptosis may significantly interfere with immune response and metabolic regulation. Meanwhile, the PI3K-Akt signaling pathway, arachidonic acid metabolism, and MAPK signaling pathway showed moderate enrichment, suggesting potential imbalances in cell proliferation, apoptosis, and inflammatory responses. Of note, virus-related pathways such as human cytomegalovirus infection and primary immunodeficiency appeared in this group, which may reflect abnormalities in the host's antiviral defense mechanism (Fig. 5c).

In the comparison of SDT + KL2 vs. NC2, the cGMP-PKG signaling pathway and cortisol synthesis and secretion emerged as the most significant pathways. This suggests disulfidptosis may exacerbate the pathological process through the hormone stress response and the intracellular second messenger system. In addition, the enrichment of ECM-receptor interaction, Antigen processing and presentation, and Epstein-Barr virus infection suggested the persistent dysregulation of extracellular matrix remodeling and immune surveillance function. Compared with SDT + KL1, the SDT + KL2 group showed unique enrichment in aldosterone/thyroid hormone synthesis, TNF signaling pathway, and antifolate resistance, suggesting the dynamic changes of disulfidptosis mechanism in different time points or samples. In general, disulfidptosis may drive the pathological process through multiple pathways such as metabolic disorders (insulin resistance, abnormal lipid metabolism), immune disorders (complement activation, cytokine release), abnormal hormone synthesis (cortisol, aldosterone), and virus-host interactions, while the differential enrichment of signaling pathways such as PI3K-Akt and cGMP-PKG further reveals the complexity of its molecular mechanism (Fig. 5d).

Expanding on these findings, the Gene Ontology (GO) enrichment analysis was conducted to delineate the functional categories associated with the differential expressed genes (DEGs). In comparing SDT + KL1 and NC1, the Wnt signaling pathway, cell differentiation, and growth factor activity pathways were significantly enriched. These pathways regulate disulfidptosis, a cell death mechanism driven by disulfide bond accumulation. They control several key processes, including protein folding, oxidative stress response, and the metabolism of sulfur-containing amino acids. Together, these processes influence the formation of protein disulfide bonds in cancer cells (Fig. S17). In a GO enrichment analysis of DEGs between NC2 and SDT + KL2, several key pathways have been identified that are particularly relevant to disulfideptosis and tumor suppression. Pathways such as endopeptidase activity and the proteasome complex are critical as they facilitate protein turnover and the removal of misfolded proteins.

Additionally, cytokine receptor binding and immune system processes enhance immune surveillance, vital for identifying and eliminating tumor cells. Furthermore, the response to oxidative stress, cell differentiation, and modulation of GTPase activity regulate the cellular redox environment and sulfur metabolism. These modifications directly influence the formation and stability of disulfide bonds within proteins, highlighting their potential impact on tumor biology (Fig. S18).

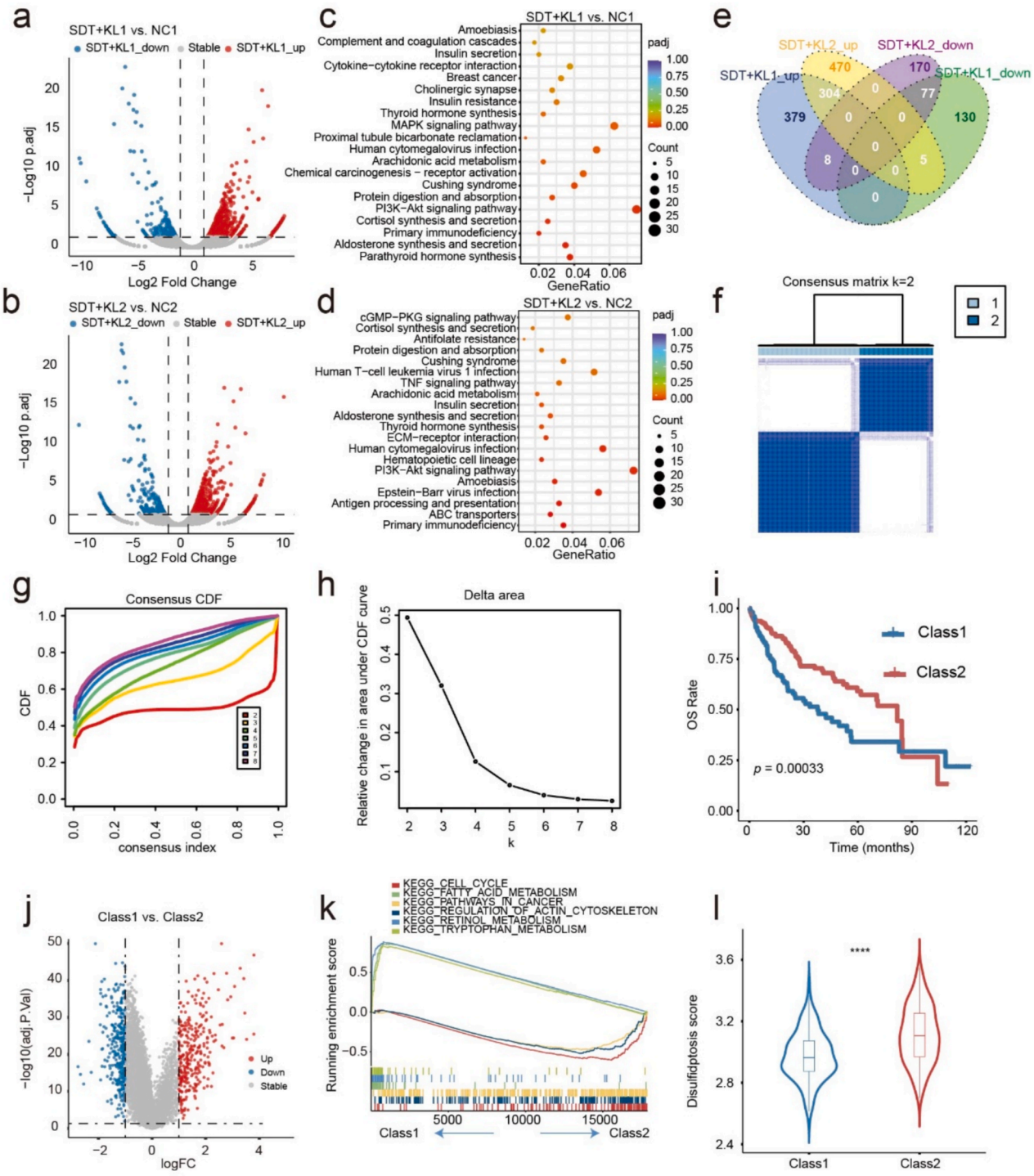

Fig. 5. Identification of disulfidptosis-associated genes and disulfidptosis subtypes. (a) Volcano plot of differentially expressed genes between SDT + KL1 and NC1. (b) Volcano plot of differentially expressed genes between SDT + KL2 and NC2. (c-d) KEGG enriched pathway. (e) Acquisition of disulfidptosis-related genes. (f) Consensus clustering matrix for k = 2. (g) CDF area curve. (h) Cumulative distribution function (CDF) curve. (i) Survival analysis of class1 and class2. (j) Differential expression genes between class 1 and class 2. (k) KEGG enrichment results. (l) Comparison of class1 and class2 disulfidptosis mortality scores.

Subsequently, according to the overlapping DEGs in the two groups (disulfidptosis-related gene, DFPRGs, Fig. 5e), we employed the DFPRGs expression in the TCGA LIHC cohort to perform unsupervised clustering and stratified LIHC patients into different disulfidptosis subtypes. The cumulative distribution function (CDF) curve may calculate the proper K value by identifying a notable rise in the area under the curve. The most stable number of clusters with minimal fluctuation within the CDF curve range may be obtained by setting the K parameter to 2. After determining that two clusters were the ideal amount based on the consensus heat map, LIHC patients were divided into two groups, class 1 and class 2 (Fig. 5f–h). Patients in the class 2 group had better prognoses than those in the class 1 group (Fig. 5i). GSEA was conducted utilizing the clusterProfiler R package for analyzing the underlying mechanisms that resulted in different results for the class 1 and class 2 groups. According to the results of KEGG enrichment, the class 2 group had a high enrichment in the retinol metabolism, cancer-related pathways, and cell

cycle, indicating that the good prognosis of class2 patients may be due to the multi-pathway synergistic effect of cell cycle normalization, metabolic homeostasis reconstruction, and immune microenvironment optimization (Fig. 5j–k). The pathway enrichment results of Hallmark and Reactome showed that cell cycle and immune checkpoint-associated pathways were also markedly enriched in class 2 groups (Fig. S19a-b). The above results indicate that the good prognosis of Class 2 patients may be due to the multi-pathway synergistic effects of cell cycle normalization, metabolic homeostasis reconstruction, and immune microenvironment optimization. In addition, this study collected multiple death-related gene sets, and the scores of multiple regulated cell deaths (RCD) were estimated by performing ssGSEA. According to the findings, the RCD scores in the class 2 group were noticeably higher than those of the class 1 group (Fig. S20). Specifically, class 2 group patients had a considerably higher disulfidptosis score versus those in the class 1 group (Fig. 5l). The above results reveal that disulfidptosis may bring new perspectives to the treatment of cancer patients.

2.7. Correlation between disulfidptosis subtypes and tumor immune microenvironment

For investigating the relationship between immunological microenvironment and disulfidptosis subtypes, immune score (Fig. 6a), stromal score (Fig. 6b), GEP score (Fig. 6c) as well as tumor purity (Fig. 6d) were calculated in this work. The outcomes presented that patients in class 1 had much lower GEP, stromal, and immune scores than those in class 2, whereas class 2 patients had considerably lower tumor purity. The immune checkpoint expression level (Fig. 6e) and cell cycle characteristic score (Fig. 6f) of patients in class 2 were higher than those in class 1. In addition, the infiltration level of various immune cells was markedly

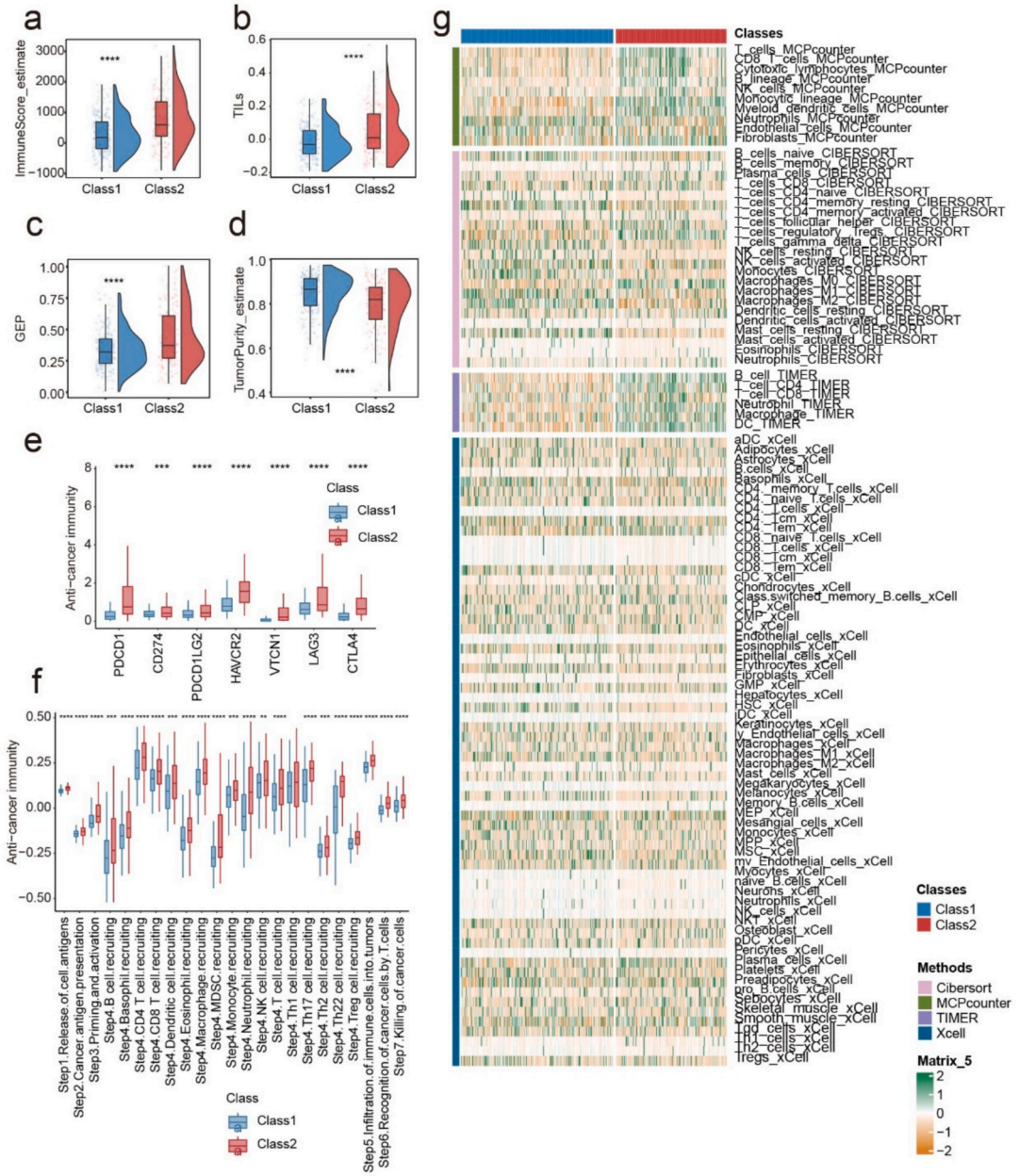

Fig. 6. Correlation between disulfidptosis subtypes and immune microenvironment. (a-d) Comparison of the immune score (a), stromal score (b), GEP (c), and tumor purity (d) between class 1 and class 2. (e) The expression levels of immune checkpoints in class 1 and 2 groups were compared. (f) Differences in the various steps of the cancer immunity cycle between class 1 and class 2. (g) The infiltration abundance of immune cells was evaluated by Cibersort, MCP-counter, TIMER, and Xcell algorithms for class 1 and class 2.

higher in the class 2 group relative to the class 1 group, encompassing neutrophils, CD8 + T cells, and other cell types with immune-killing functions. The above results provide additional evidence to support disulfidptosis-induced immunogenic cancer cell death.

2.8. Establishment and validation of prognostic model

In this study, two machine learning algorithms, LASSO regression (Fig. 7a and b) and random forest (Fig. 7c and d), were used to refine the selection of signature genes and mitigate the risk of overfitting. A total of 5 genes were identified (Fig. 7e, table S1), and then multivariate Cox regression analysis was performed, incorporating each prognostic gene to obtain the regression coefficient of each gene. Subsequently, a risk scoring model was developed based on the activity of the five characterized genes, weighted by their respective multivariate Cox proportional hazards regression coefficients. Based on the median risk score for survival analysis, the TCGA LIHC patients were split into low- and high-risk groups. The results indicated that the overall survival rate of the high-risk group in TCGA cohort was much lower than that of the low-risk group (Fig. 7f). The time-dependent ROC results showed that the AUCs of TCGA LIHC patients at 1, 2, 3, and 4 years were 0.74, 0.74, 0.75, and 0.72, separately (Fig. 7g). The survival analysis in GSE14520 cohort also demonstrated that patients in high-risk group had a considerably worse prognostic ability versus those in the low-risk group (Fig. 7h). Time-dependent ROC results revealed that at 1, 2, 3, and 4 years, the AUCs were respectively, 0.61, 0.64, 0.67, and 0.66 (Fig. 7i). The findings above present the model's ability to forecast prognoses of patients with LIHC accurately.

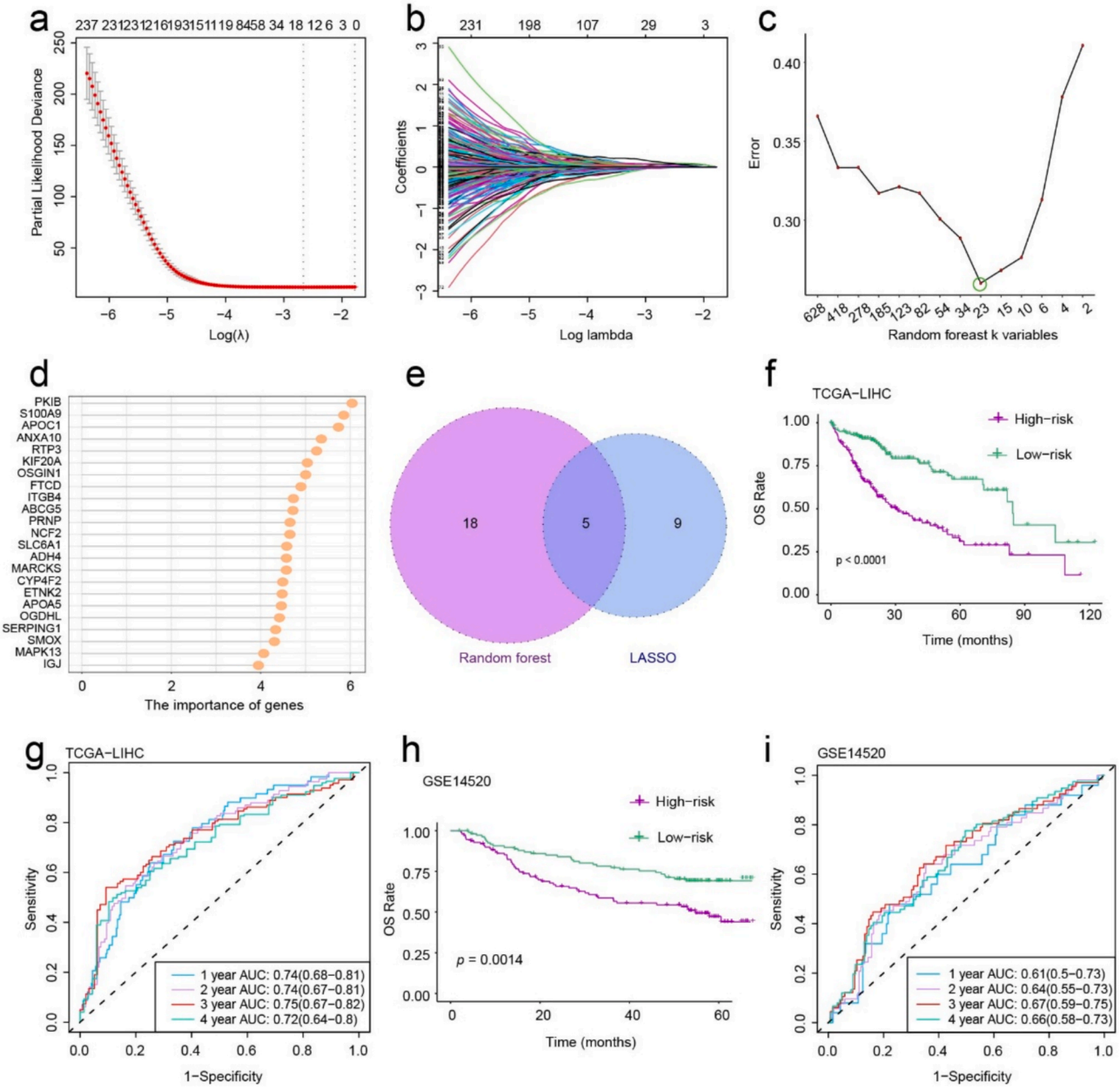

Fig. 7. Construction of a prognostic risk score. (a) LASSO coefficient values of the candidate genes. The vertical dashed lines are the optimal log(λ) values. (b) Candidate genes profiles based on LASSO coefficients. (c) The retained genes estimate the generalization error of the random forest classification algorithm after each deletion. (d) Importance of prognosis-related genes identified by random forest. (e) LASSO and random forest identified five prognosis-related genes. (f) Kaplan-Meier curves for overall survival (OS) in TCGA LIHC cohort. (g) ROC curve of the risk scoring model in TCGA-LIHC cohort. (h) Kaplan-Meier curves for overall survival (OS) in the GSE14520 cohort. (i) ROC curve of the risk scoring model in the GSE14520 cohort.

3. Conclusion

Disulfidptosis is a potential new approach to promote the death of tumor cells. Here, we report an effective new method to enhance disulfidptosis in combination with SDT to prevent tumor occurrence, development, and metastasis. NBs were synthesized by thin film hydration method and then co-assembled with KL and ICG to obtain nanoparticles ICG@C3F8-KL NBs, which can be degraded and produce a large amount of ROS under ultrasound irradiation. This process leads to the rupture of ICG@C3F8-KL NBs and the release of KL. This sonodynamic therapy-enhanced disulfidptosis can effectively inhibit glucose uptake, reduce NADPH synthesis, and promote depletion. In addition, this study exhibited a strong link between the immune microenvironment and disulfidptosis, metabolic abnormalities, and pathological processes of LIHC by comprehensively analyzing the differentially expressed genes of disulfidptosis subtypes in the TCGA cohort. Through KEGG and GO enrichment analysis of differentially expressed genes, we found that disulfidptosis may drive tumor progression through the synergistic effects of multiple signaling pathways, including immune response, metabolic regulation, cell cycle, hormone synthesis, etc. In particular, the enrichment of pathways such as complement and coagulation cascade, insulin secretion, and cytokine-cytokine receptor interaction indicated that disulfidptosis not only affects the metabolic state of tumor cells but may also improve the tumor immune microenvironment by inducing immunogenic death. Through machine learning methods (LASSO and random forest), we developed a predictive model that accurately predicts the prognosis of patients with LIHC via applying genes linked to disulfidptosis. The survival analysis findings in both external validation sets and TCGA demonstrated the model's high prediction performance, supporting the prognostic evaluation and personalized treatment of liver cancer.

In summary, this paper proposes a nanomedicine that effectively utilizes sonodynamics to enhance disulfidptosis and deeply clarifies the potential mechanism of disulfidptosis in LIHC. It also suggests its possibility as a new target for LIHC immunotherapy, laying the groundwork for future clinical applications.

4. Materials and methods

4.1. Expression of SLC7A11 in LIHC

Utilizing the GEPIA database (https://gepia2.cancer-pku.cn/#analysis), we investigated the differences in the expression of SLC7A11 between normal and LIHC patients. The TCGA database supplied the tumor and normal tissue information, which was assessed online using the GEPIA database. To determine whether LIHC and normal tissues express SLC7A11 differently, 369 instances of LIHC and 160 cases of normal were acquired to identify the differential expression of SLC7A11 in normal and LIHC tissues.

4.2. Materials

Avanti Polar Lipids (Alabaster, AL) supplied the 1.2-Distearoyl-*sn*-glycerol-3-phosphocholine (DSPC) and 1.2-stearoyl-*sn*-glycerol-3-phosphoethanolamine-N-(methoxy [polyethylene glycol]-2000) (DSPE-PEG-2000). ICG was provided by Shanghai Yuan Ye Bio-Technology Co., Ltd., located in Shanghai, China. The CCK-8 cell counting kit was obtained from BD Pharmingen. KL-11743 (KL) was supplied by Shanghai MCE Chemicals Technology (Shanghai, China).

4.3. Synthesis of ICG@C3F8-KL NBs

According to previous publications, [35] we produced ICG@C3F8-KL NBs by applying the thin-film hydration ultrasonic process. DSPE-PEG-2000 and DSPC should first be combined in a 1:9 mass ratio. Then, in a 2:1 vol/vol solution of methylene chloride and methanol, 95.7 μL of 10 mM KL was incorporated. After thoroughly mixing and dissolving the previously described solution, transfer it to a beaker and let it evaporate to form a lipid layer. 5 ml of 100 μg/mL ICG in PBS was applied to create a lipid solution of the dried film (KL:ICG (mass ratio) = 1:1). Subsequently, a microextruder (Avanti Polar Lipids, Alabaster, AL) was exploited to extrude the suspension 20 times through 200 nm and 100 nm membranes. The squeezed solution was then moved to a sealed vial once the syringe had been drained and loaded with C3F8. Following a 60-second physical agitation in a dental mixer (manufactured by YJT Medical Apparatus and Instruments, Shanghai, China), the mixture was resuspended in 2 ml of PBS solution and kept at 4 °C. Each process is carried out in a dark environment. Without KL, nanobubbles were produced using the same process.

4.4. Characterization of ICG@C3F8-KL NBs

The PDI value, zeta potential, and particle size of nanomedicine were ascertained via the DLS (Malvern, UK) method. The stability of NBs in both water and cell culture medium were evaluated by observing size changes over seven days. The morphology of ICG@C3F8-KL NBs and ICG@C3F8 NBs was observed via transmission electron microscopy (TEM, JEOL, Japan) and scanning electron microscopy (SEM, JEOL JSM-6700F). UV–vis spectrometer (SHIMADZU, Japan) and fourier transform infrared (FT-IR) spectroscopy were exploited to record absorption spectra of ICG@C3F8-KL NBs, ICG, and KL.

4.5. Loading of KL into ICG@C3F8-KL NBs

The drug loading rates and entrapment efficiency rates were tested by UV–vis spectrometer. These measurements were then used to calculate the loading efficiency (LE %) and loading content (LC %).

LE (%) = W_loaded/W_total × 100 %.

LC (%) = W_loaded/ (W_loaded + W_polymer) × 100 %.

Wtotal: Total weight of the drug added.

W_loaded: Weight of the drug encapsulated in the nanoparticles.

W_polymer: Weight of the polymer used.

Encapsulation Efficiency (LE) and Loading Content (LC) for KL.

4.6. Drug administration ratios and cell viability assessment

To evaluate the effect of different drug administration ratios on treatment outcomes, we established several drug combinations with varying ratios of ICG to KL, including 1:1, 2:1, 1:2, 3:1, and 1:3. In these experiments, the total drug loading and concentration in the nanobubbles were kept constant, and only the drug dosing ratio was adjusted. To assess the therapeutic effect of different drug ratios, we performed CCK-8 (cell counting kit-8) assays to measure cell viability. Briefly, cells were seeded in 96-well plates and different drug solutions with varying ratios were then added to the wells, and cells were treated for 24 h. After treatment, CCK-8 reagent was added, and cells were incubated for an additional 2 h. The absorbance was measured at 450 nm using a microplate reader. The cell viability was compared across different drug ratio groups to determine the optimal drug combination for treatment.

4.7. In vitro drug release kinetics under ultrasound stimulation

To further evaluate the release behavior of ICG and KL under ultrasound (US) irradiation, an in vitro drug release assay was performed. Briefly, ICG@C_3F_8-KL NBs were individually loaded into dialysis bags (MWCO = 3.5 kDa) and immersed in 10 mL of phosphate-buffered saline (PBS, pH 7.4). All samples were incubated at 37 °C with gentle shaking (100 rpm). Two experimental conditions were established: one group was incubated without US exposure (No US), while the other was subjected to ultrasound stimulation (1.0 W/cm^2, 1 MHz, 50 % duty cycle, 30s) before incubation. At predetermined time points (0, 1, 2, 4, 8, 12, 24, 48, and 72 h), 500 μL of the external solution was withdrawn and

replaced with an equal volume of fresh PBS. The absorbance of ICG and KL at 780 nm and 247 nm, respectively, was measured using a UV–Vis spectrophotometer to quantify the cumulative drug release.

4.8. In vitro ROS generation of ICG@C3F8-KL NBs upon ultrasound radiation

A solution of Single Online State Oxygen Sensor Green Fluorescent Probe (SOSG) (5 nM final working concentration) was incorporated into the ICG@C3F8-KL NBs, ICG@C3F8 NBs, NBs and ICG in a 6-well plate and mixed completely. Afterward, the mixture was activated using ultrasonic treatment equipment. This equipment was utilized in all experiments in this study. For three minutes, the ultrasonic parameters were set to 1.0 W/cm^2, 1.0 MHz, and a 50 % duty cycle. The fluorescence spectrum of SOSG was then measured using a fluorescence spectrophotometer (Cary5000, Malaysia) to detect the formation of singlet oxygen ($^1O_2$).

4.9. Cell culture

Human hepatocellular carcinoma cell line (HepG2) along with Murine hepatocellular carcinoma cell line (Hepa 1–6/luc) were supplied by Procell Life Technologies Co., Ltd. (Wu Han, China) and cultured in DMEM media containing 10 % FBS in a humid incubator at 37 ℃ with 5 % CO_2.

4.10. Cytotoxicity of therapeutic effect in vitro

A CCK-8 test was conducted to evaluate the cytotoxicity in HepG2 cells. After being seeded at 1×10^4 cells per well in 96-well plates, the cells were grown for 24 h. Afterward, cells were treated by ICG@C3F8-KL NBs, ICG@C3F8 NBs and KL upon ultrasound radiation (1.0 W/cm^2, 50 % duty cycle, 30 s, 1 MHz following treatment for 4 h), ICG@C3F8-KL NBs upon ultrasound radiation (1.0 W/cm^2, 50 % duty cycle, 30 s, 1 MHz following treatment for 4 h) at final KL concentrations ranging from 5, 10, 20, 40, 80, 160, 320, 640 to 1280 μM for 24 h, respectively. Then, 10 μL CCK-8 was added to the wells. A microplate reader measured the absorbance of each well at 450 nm (peak absorbance). The experiment was performed in triplicates.

4.11. Intracellular production of ROS in ICG@C3F8-KL NBs cells during ultrasound radiation

The intracellular level of ROS was examined by employing DCFH-DA as a fluorescent probe. In brief, cells (2×10^5 cells) in 1 ml complete media were incorporated into each well on a 24-well plate and inoculated at 37 °C for 24 h. Spheroids were subsequently treated through ICG@C3F8 NBs + US (SDT group), ICG@C3F8-KL NBs, ICG@C3F8-KL NBs + US (SDT + KL), and KL, separately, for 4 h (KL concentration = 67.72 μM). The group of cells that underwent no treatment served as a negative control. Subsequently, the culture medium of the cells was replaced with a serum-free medium and then incubated with ROS indicator DCFH-DA (10 μM) for 30 mins. After being cleaned twice by PBS, cells were exposed to ultrasound radiation (1.0 W/cm^2, 50 % duty cycle, 30 s, 1 MHz) or not. Afterward, the cell nuclei were stained in DAPI. Fluorescence microscopy was then applied to gather images.

4.12. Mitochondrial membrane potential staining by JC-1 assay

To assess the impact of ROS on mitochondrial function, we performed mitochondrial membrane potential (ΔΨm) analysis using JC-1 staining. Briefly, cells were treated under ICG@C3F8 NBs + US (SDT group), ICG@C3F8-KL NBs, ICG@C3F8-KL NBs + US (SDT + KL), and KL, separately, for 4 h (KL concentration = 67.72 μM). The group of cells that underwent no treatment served as a negative control. Subsequently, the culture medium of the cells was replaced with a serum-free medium and then incubated with ROS indicator JC-1 dye for 30 mins. After being cleaned twice by PBS, cells were exposed to ultrasound radiation (1.0 W/cm2, 50 % duty cycle, 30 s, 1 MHz) or not. Afterward, the cell nuclei were stained in DAPI. Fluorescence microscopy was then applied to gather images. In fluorescence microscopy, a shift from red fluorescence (JC-1 aggregates, indicative of healthy mitochondria) to green fluorescence (JC-1 monomers, indicative of mitochondrial depolarization) was observed.

4.13. Live/dead cell staining

On 96-well plates, 1×10^4 HepG2 cells were planted per well. Following a 24-hour incubation period, cells were subjected to various drug treatments and 48 h of ultrasonic radiation (1.0 W/cm^2, 50 % duty cycle, 30 s, 1 MHz, KL concentration = 67.72 μM). After that, the treated cells were left in the cell culture container for 30 min to be stained with a PBS solution containing PI and Calcein-AM. The cell samples were observed utilizing fluorescence microscopy at the excitation of 488 nm and 532 nm following PBS washing.

4.14. Wound healing and transwell

Transwell and the wound healing experiment were implemented to examine cell migration. In short, a sterile pipette tip was utilized to create the scratches after HepG2 cells were seeded onto 6-well plates. Cells were then cultivated in DMEM media devoid of FBS. After 24 h, cells were treated with different drug treatments and ultrasound radiation (1.0 W/cm^2, 50 % duty cycle, 30 s, 1 MHz, KL concentration = 67.72 μM) for 24 h. Subsequently, the migration distance was recorded. For the transwell assay, the upper chamber, equipped with an 8 μm pore size filter, was used, and the bottom chamber was filled with 600 μL of complete DMEM. Cells were exposed to various drug treatments and ultrasonic radiation (1.0 W/cm^2, 50 % duty cycle, 30 s, 1 MHz, KL concentration = 67.72 μM) for 24 h after 24 h. Crystal violet was then utilized to stain the migratory cells.

4.15. Colony formation assay

HepG2 cells were cultivated for 24 h after being seeded onto 6-well plates in quantities of 2000 cells each. The cells were then exposed to ultrasonic radiation (1.0 W/cm^2, 50 % duty cycle, 30 s, 1 MHz, KL concentration = 67.72 μM) for 12 days while being incubated with ICG@C3F8 NBs + US (SDT group), ICG@C3F8-KL NBs, ICG@C3F8-KL NBs + US (SDT + KL) and KL. The cells were fixed with 70 % ethyl alcohol and rinsed with PBS once they had grown into visible colonies. The colonized cells were dyed with 0.5 % crystal violet, and a camera was applied to photograph the colonies.

4.16. Cell intake of glucose

A glucose assay kit (S0201S, Beyotime) was used to evaluate cell uptake of glucose. HepG2 cells were inoculated on 6-well plates at 1×10^6 cells per well. Cells were exposed to various drug treatments and ultrasonic radiation (1.0 W/cm^2, 50 % duty cycle, 30 s, 1 MHz, KL concentration = 67.72 μM) for 24 h following incubation for 24 h. The cells were gathered and mixed with the tissue lysate (for glucose), and then the supernatants were obtained as the samples to be tested. Standard curves were prepared using the standards, and the glucose content of the samples to be tested was determined. A microplate reader (SpectraMax) was exploited to measure the absorbance of the wells at 630 nm (peak absorbance). Lastly, the bicinchoninic acid (BCA) protein assay kit was employed to determine the concentration of protein, and the glucose content per unit of protein in the sample was computed. The experiment was performed in triplicates.

4.17. Detection of the intracellular NADP+/NADPH ratio

NADP+/NADPH assay kit (S0179, Beyotime) was used to evaluate the intracellular NADP+/NADPH ratio. HepG2 cells were seeded on 6-well plates at 1×10^6 cells per well. After 24 h incubation, cells were treated with the different drug treatments and ultrasound radiation (1.0 W/cm^2, 50 % duty cycle, 30 s, 1 MHz, KL concentration = 67.72 μM) for 12 h. NADP+/NADPH extract was incorporated after being rinsed with PBS and then gently blown to facilitate cell lysis. Centrifugation was then performed at 4 °C and 12,000 g for 5 min, and the supernatants were collected as samples for testing. Subsequently, 50 μL of the sample was pipetted into a 96-well plate for measurement. Afterwards, 100 μL of G6PDH working solution was added and incubated for 10 min at 37 °C, protected from light. Subsequently, 10 μL of color development solution was added, and the total amount of NADPH and NADP + was measured at 450 nm (peak absorbance) using a microplate reader (SpectraMax). Next, the sample to be tested was heated in a 60 °C water bath for 30 min to remove NADP+, resulting in a new sample for testing. The amount of NADPH was then measured using the same method described above. Finally, the protein concentration was determined using a BCA protein assay kit, and the NADP+/NADPH ratio was calculated.

4.18. Detection of the expression of F-actin

HepG2 cells were inoculated at 1×10^5 cells per well on 24-well plates. Cells were exposed to various drug treatments and ultrasonic radiation (1.0 W/cm^2, 50 % duty cycle, 30 s, 1 MHz, KL concentration = 67.72 μM) for 12 h following incubation for 24 h. Following a PBS wash, the cells were fixed with 4 % paraformaldehyde for 10 min at ambient temperature. The aforementioned fixed cells were then incubated for 30 min at ambient temperature in the dark following PBS washing with DAPI (Blue) and F-actin (Green) and then observed by CLSM.

4.19. Western blot

Western blot analysis was performed to evaluate the levels of SLC7A11 in HepG2 and Hepa 1–6/luc cells. To evaluate occurrence of disulfidptosis, HepG2 cells were inoculated on 6-well plates at 1×10^6 cells per well. Cells were exposed to various drug treatments (PBS, ICG@C3F8 NBs + US (SDT group), ICG@C3F8-KL NBs, ICG@C3F8-KL NBs + US (SDT + KL), ICG@C3F8 NBs + US (SDT group), ICG@C3F8-KL NBs, ICG@C3F8-KL NBs + DTT + US (SDT + KL + DTT) and KL for 24 h. The ultrasonic radiation was 1.0 W/cm^2, 50 % duty cycle, 30 s, 1 MHz, KL concentration = 67.72 μM, DTT concentration = 5 mM). Following treatment, the cells underwent three PBS washes for WB to measure the expression of FLNA, TLN1, and MYH9 proteins (Immunoway Biotechnology Co. LTD).

4.20. Rna-seq analysis

4.20.1. Data collection

TCGA-LIHC transcriptome data, along with the corresponding clinical information, were downloaded from TCGA (https://cancergenome.nih.gov). Gene expression profiles of the transcriptome of GSE14520 and corresponding clinical data were derived from GEO (https://www.ncbi.nlm.nih.gov/geo/).

4.20.2. Differentially expressed genes (DEGs) analysis

The edgeR R package was used to identify differentially expressed genes (DEGs) between the treatment and control groups (group SDT + KL1 vs. NC1, group SDT + KL2 vs. NC2), with screening criteria of $|\log2FC| > 1$ and p.adjust < 0.05. The overlapping DEGs of the two groups of differential genes were called disulfide apoptosis-related genes (DFPRGs) for subsequent analysis.

4.20.3. Identification of disulfidptosis subtypes

We obtained the expression levels of DFPRGs in LIHC from the TCGA cohort for subsequent analysis. To identify the disulfidptosis subtypes (class1/class2), hierarchical clustering of LIHC was performed according to the DFPRGS expression pattern in each sample. The analysis was implemented employing the unsupervised clustering "Pam" method based on the Pearson and Ward linkage, realized with the software package "ConsensusClusterPlus"R [36].

4.20.4. Gene set enrichment analysis (GSEA)

A GSEA was conducted to investigate the possible mechanisms of the disulfidptosis subtypes. Gene sets containing KEGG, broad hallmarks, and Reactome pathways were obtained from the MSigDB database of Broad Institute. The genes with varying expression levels in the class 1 and class 2 groups were then employed to create a ranked gene list. GSEA was carried out utilizing the clusterProfiler R package with 1000 permutations [37]. Afterward, the multiple tests were adjusted to control for FDR with the Benjamini-Hochberg procedure.

4.20.5. Correlation between disulfidptosis subtypes and tumor infiltration microenvironment

To analyze the association between tumor immune infiltration and disulfidptosis subtypes, this study quantified immune infiltration scores using four methods: MCP-counter, Cibersort, TIMER, and xCell, implemented via the IOBR R package [38]. Additionally, the ESTIMATE R package was used to calculate the stromal and immune scores of LIHC. The response to PD-1 blockade was then predicted by GSEA using an 18-gene T cell inflammatory gene expression profile (GEP).

4.20.6. Construction and validation of prognostic models

To identify genes associated with disulfidptosis subtypes, we first divided LIHC patients into class 1 and 2 groups. We then used the limma R package [39] to determine DEGs. The genes with an adjusted p-value of less than 0.05 by the Benjamin and Hochberg were determined to be genes that were significantly different between both disulfiram subtypes. Genes linked to prognosis were then screened through two machine learning approaches. Specifically, (1) LASSO regression was utilized to filter the genes with the optimal prediction results, thus narrowing the range of candidate genes, and the regression shrinkage parameter was determined using 10-fold cross-validation. (2) The random forest method was used to screen features. First, a certain number of samples (called the in-bag sample set) were selected from the sample set to train the decision tree in the random forest. This method constructed 10,000 decision trees, and a certain number of genes were randomly selected as classification features when constructing each decision tree. A trained random forest model was then used to predict the out-of-bag samples and evaluate the classification's generalization error. Additionally, it is crucial that the classifier can estimate the importance score of each gene feature by predicting the out-of-bag samples. In each iteration, we selected one-third of the least important genes for removal to eliminate redundant information and effectively reduce the number of features used to build the model. After each gene deletion, we recalculated the model's generalization error for classifying the out-of-bag samples. To create a predictive model based on the specific activity profile of the genes in the sample, we first employed 628 important genes as features. Next, we observed a minor variation in the model's generalization error after each deletion of one-third of the least important gene features. However, the error increased dramatically when fewer than 23 genes were retained. Therefore, 23 genes relevant to prognostic classification were selected from the 628 important genes. Subsequently, we conducted multivariate Cox proportional hazards regression analyses on the overlapping genes identified by random forest and LASSO. We developed a disulfidptosis-related prognostic risk scoring model as follows: $riskscore = \sum \beta_i \times E_i$, where β_i is the coefficient of gene i in the multivariate Cox, E_i representing the expression of gene i. According to the median risk score, LIHC samples can be

separated into two groups: high risk (≥ median) or low risk (< median). Kaplan-Meier curves were exploited for survival analysis, and the log-rank test was applied to compute p-values, which estimated the survival distribution of the two subgroups. The external validation cohort from the GEO database confirmed the strong predictive performance of the risk score model for patient prognosis.

4.21. Establishment of Hepa1-6/luc mouse xenograft model

The mice received a subcutaneous injection of 1.5×10^6 Hepa1-6/luc cells utilizing a 100 μL solution of Matrigel and saline (1:1, v/v). The tumor sizes of the mice increased to about 100 mm^3 after a week.

4.22. Biodistribution in Hepa1-6/luc mouse xenograft model

Hepa 1–6/luc tumor-bearing C57BL/6 mice were then intravenously injected with 200 μL of free ICG and ICG@C3F8-KL NBs in PBS, separately, along with the same dose of ICG for in vivo imaging.The biodistribution of major organs and ex vivo fluorescent images, along with their quantification data 48 h after injection, provided additional confirmation of the tumor.

4.23. Inhibition of tumor growth in a Hepa1-6/luc mouse xenograft model

To assess the antitumor efficacy of ICG@C3F8-KL NBs in combination with ultrasound (US), an in vivo tumor model was established using C57BL/6J mice. Once the tumors reached approximately 100 mm^3 in volume, mice were randomly divided into five groups: (1) PBS, (2) ICG@C3F8-KL NBs, (3) KL, (4) SDT, and (5) SDT + KL. For treatment, mice received intravenous injections of ICG@C_3F_8-KL NBs (dose: X mg/kg) every two days. In the US-treated groups, ultrasound irradiation (1.0 W/cm^2, 1 MHz, 50 % duty cycle, 2 min) was applied 4 h post-injection. Tumor volume was measured every four days using a digital caliper and calculated as $V = (\text{length} \times \text{width}^2) / 2$. On day 20, IVIS (AniView SE, Guangzhou Biolight Biotechnology Co., Ltd) was used to calculate bioluminescence signals of tumors in vivo and then mice were euthanized, and tumors were excised, weighed, and subjected to histological analysis.

To further evaluate the therapeutic mechanism, tumor sections were analyzed using TUNEL staining to assess apoptosis and Ki-67 immunofluorescence staining to evaluate cell proliferation. Stained sections were visualized under a fluorescence microscope.

To assess the potential systemic toxicity of the NBs, body weights were taken and recorded every four days, and liver and kidney function markers were evaluated by blood samples post-treatment. Serum levels of alanine aminotransferase (ALT), aspartate aminotransferase (AST), blood urea nitrogen (BUN), and creatinine (CRE) were measured.

4.24. Histopathological analysis

The solid tumors were harvested from tumor-bearing mice of tumor inoculation for histological observation by standard hematoxylin and eosin (H&E) staining. For H&E staining, the excised tumor and organs were fixed in a 4 % paraformaldehyde solution, embedded in paraffin, sectioned, and stained with H&E.

4.25. Statistical analysis

For all statistical studies, GraphPad Prism 8.0.1 (GraphPad Software) was utilized. Normalization or transformation was used as a preprocessing technique for the raw data. Unless indicated in the figure legend, data are expressed as the mean ± SD from at least three independent biological replicates. When comparing more than two or multiple groups, one-way or two-way analysis of variance (ANOVA) together with Tukey post-hoc tests were employed, whereas an unpaired two-sided *t*-test was utilized between the two groups. Each figure or experiment has a caption that explains the number of independent repetitions, type of test, and significance level. The significance level was set at $p < 0.05$. $^*p < 0.05$, $^{**}p < 0.01$, $^{***}p < 0.001$, $^{****}p < 0.0001$.

CRediT authorship contribution statement

Yichi Chen: Investigation. **Xin Lin:** Investigation. **Jiayue Qiu:** Investigation. **Yucao Sun:** Investigation. **Bolin Wu:** Investigation. **Haitao Shang:** Investigation. **Liwen Deng:** Investigation. **Xi Wang:** Conceptualization. **Nanxing Li:** Investigation. **Chen Huang:** Investigation. **Tianhong Zhang:** Methodology, Funding acquisition. **Zhiguang Wu:** Conceptualization. **Gang Hou:** Conceptualization. **Xiaohui Yan:** Investigation. **Shoufeng Wang:** Conceptualization. **Wen Cheng:** Investigation, Conceptualization.

Declaration of competing interest

The authors declare that they have no known competing financial interests or personal relationships that could have appeared to influence the work reported in this paper.

Acknowledgments

The authors would like to express their sincere gratitude for the support from the National Natural Science Foundation of China (No. 82171947, No. 52375565), the Macao Science and Technology Development Fund (002/2023/ALC), the Science and Technology Development Fund, Macau SAR (File no. 006/2023/SKL), the General Research Grants of Macau university of Science and Technology (FRG-21-032-SKL), the Macao Science and Technology Development Fund (002/2023/ALC), State Key Laboratory of Robotics (2019-O02), State Key Laboratory of Systems Medicine for Cancer (KF2420-93), and Fundamental Research Funds for Central Universities.

Appendix A. Supplementary data

Supplementary data to this article can be found online at https://doi.org/10.1016/j.ultsonch.2025.107368.

References

[1] X. Liu, L. Nie, Y. Zhang, Y. Yan, C. Wang, M. Colic, K. Olszewski, A. Horbath, X. Chen, G. Lei, C. Mao, S. Wu, L. Zhuang, M.V. Poyurovsky, M. James You, T. Hart, D.D. Billadeau, J. Chen, B. Gan, Actin cytoskeleton vulnerability to disulfide stress mediates disulfidptosis, Nat. Cell Biol. 25 (2023) 404–414.
[2] G. Zhao, Y. Jiang, Y. Wang, S. Wang, N. Li, Comprehensive characterization of cell disulfidptosis in human cancers: An integrated pan-cancer analysis, Genes Diseases 11 (2024) 101095.
[3] S. Zhou, J. Liu, A. Wan, Y. Zhang, X. Qi, Epigenetic regulation of diverse cell death modalities in cancer: a focus on pyroptosis, ferroptosis, cuproptosis, and disulfidptosis, J. Hematol. Oncol. 17 (2024) 22.
[4] C. Mao, M. Wang, L. Zhuang, B. Gan, Metabolic cell death in cancer: ferroptosis, cuproptosis, disulfidptosis, and beyond, Protein Cell 15 (2024) 642–660.
[5] X. Liu, L. Zhuang, B. Gan, Disulfidptosis: disulfide stress-induced cell death, Trends Cell Biol. 34 (2024) 327–337.
[6] T. Zheng, Q. Liu, F. Xing, C. Zeng, W. Wang, Disulfidptosis: a new form of programmed cell death, Journal of Experimental & Clinical Cancer Research : CR 42 (2023) 137.
[7] D. Jin, Y. Zhu, M. Liu, W. Yu, J. Yu, X. Zheng, L. Wang, Y. Wu, K. Wei, J. Cheng, Y. Liu, A leaking-proof theranostic nanoplatform for tumor-targeted and dual-modality imaging-guided photodynamic therapy, BME Front. 4 (2023) 0015.
[8] L. Wu, Y. Jin, X. Zhao, K. Tang, Y. Zhao, L. Tong, X. Yu, K. Xiong, C. Luo, J. Zhu, F. Wang, Z. Zeng, D. Pan, Tumor aerobic glycolysis confers immune evasion through modulating sensitivity to T cell-mediated bystander killing via TNF-α, Cell Metab. 35 (2023) 1580–1596.e1589.
[9] D. Abrahami, H. Tesfaye, H. Yin, S. Vine, B. Hicks, O.H.Y. Yu, L. Campeau, R. W. Platt, S. Schneeweiss, E. Patorno, L. Azoulay, Sodium-glucose cotransporter 2 inhibitors and the short-term risk of bladder cancer: An international multisite cohort study, Diabetes Care 45 (2022) 2907–2917.
[10] J. Afonso, L.L. Santos, A. Longatto-Filho, F. Baltazar, Competitive glucose metabolism as a target to boost bladder cancer immunotherapy, Nat. Rev. Urol. 17 (2020) 77–106.

[11] T. Wang, Z. Liu, X. Wang, P. Bai, A. Sun, Z. Shao, R. Luo, Z. Wu, K. Zhang, W. Li, W. Xiao, B. Duan, Y. Wang, B. Chen, J. Xing, Identification of potential therapeutic targets in urothelial bladder carcinoma of Chinese population by targeted next-generation sequencing, Cancer Biol. Ther. 21 (2020) 709–716.
[12] E.G. Konstantakou, G.E. Voutsinas, A.D. Velentzas, A.S. Basogianni, E. Paronis, E. Balafas, N. Kostomitsopoulos, K.N. Syrigos, E. Anastasiadou, D.J. Stravopodis, 3-BrPA eliminates human bladder cancer cells with highly oncogenic signatures via engagement of specific death programs and perturbation of multiple signaling and metabolic determinants, Mol. Cancer 14 (2015) 135.
[13] X. Jin, W. Jin, L. Tong, J. Zhao, L. Zhang, N. Lin, Therapeutic strategies of targeting non-apoptotic regulated cell death (RCD) with small-molecule compounds in cancer, Acta Pharm. Sin. B 14 (2024) 2815–2853.
[14] Q. Wu, W. Ba-Alawi, G. Deblois, J. Cruickshank, S. Duan, E. Lima-Fernandes, J. Haight, S.A.M. Tonekaboni, A.M. Fortier, H. Kuasne, T.D. McKee, H. Mahmoud, M. Kushida, S. Cameron, N. Dogan-Artun, W. Chen, Y. Nie, L.X. Zhang, R. N. Vellanki, S. Zhou, P. Prinos, B.G. Wouters, P.B. Dirks, S.J. Done, M. Park, D. W. Cescon, B. Haibe-Kains, M. Lupien, C.H. Arrowsmith, GLUT1 inhibition blocks growth of RB1-positive triple negative breast cancer, Nat. Commun. 11 (2020) 4205.
[15] Y. Wang, Y. Jiang, D. Wei, P. Singh, Y. Yu, T. Lee, L. Zhang, H.K. Mandl, A. S. Piotrowski-Daspit, X. Chen, F. Li, X. Li, Y. Cheng, A. Josowitz, F. Yang, Y. Zhao, F. Wang, Z. Zhao, A. Huttner, R.S. Bindra, H. Xiao, W. Mark Saltzman, Nanoparticle-mediated convection-enhanced delivery of a DNA intercalator to gliomas circumvents temozolomide resistance, Nat. Biomed. Eng. 5 (2021) 1048–1058.
[16] R. Kaur, A. Bhardwaj, S. Gupta, Cancer treatment therapies: traditional to modern approaches to combat cancers, Mol. Biol. Rep. 50 (2023) 9663–9676.
[17] J. Tu, A.C.H. Yu, Ultrasound-mediated drug delivery: Sonoporation mechanisms, Biophys., Critical Factors, BME Frontiers 2022 (2022) 9807347.
[18] C. Yang, Y. Yang, Y. Li, Q. Ni, J. Li, Radiotherapy-triggered proteolysis targeting chimera prodrug activation in tumors, J. Am. Chem. Soc. 145 (2023) 385–391.
[19] D. Tang, H. Zhou, M. Cui, G. Liang, H. Zhang, H., Xiao, NIR-II light accelerated prodrug reduction of Pt(IV)-incorporating pseudo semiconducting polymers for robust degradation and maximized photothermal/chemo-immunotherapy,, Adv. Mater. (Deerfield Beach Fla.), 35 (2023) e2300048.
[20] Y.I. Yoon, T.J. Yoon, H.J. Lee, Optimization of ultrasound parameters for microbubble-nanoliposome complex-mediated delivery, Ultrasonography (seoul, Korea) 34 (2015) 297–303.
[21] G. Liang, N. Montesdeoca, D. Tang, B. Wang, H. Xiao, J. Karges, K. Shang, Facile one-pot synthesis of Ir(III) Bodipy polymeric gemini nanoparticles for tumor selective NIR photoactivated anticancer therapy, Biomaterials 309 (2024) 122618.
[22] G. Liang, W. Cao, D. Tang, H. Zhang, Y. Yu, J. Ding, J. Karges, H. Xiao, Nanomedomics, ACS Nano 18 (2024) 10979–11024.
[23] M. Cui, D. Tang, B. Wang, H. Zhang, G. Liang, H. Xiao, Bioorthogonal guided activation of cGAS-STING by AIE photosensitizer nanoparticles for targeted tumor therapy and imaging,, Adv. Mater. (Deerfield Beach Fla.), 35 (2023) e2305668.
[24] H. Zhou, D. Tang, X. Kang, H. Yuan, Y. Yu, X. Xiong, N. Wu, F. Chen, X. Wang, H. Xiao, D. Zhou, Degradable Pseudo Conjugated Polymer Nanoparticles with NIR-II Photothermal Effect and Cationic Quaternary Phosphonium Structural Bacteriostasis for Anti-Infection Therapy, Advanced science (Weinheim, Baden-Wurttemberg, Germany), 9 (2022) e2200732.
[25] D. Guo, Y. Tong, X. Jiang, Y. Meng, H. Jiang, L. Du, Q. Wu, S. Li, S. Luo, M. Li, L. Xiao, H. He, X. He, Q. Yu, J. Fang, Z. Lu, Aerobic glycolysis promotes tumor immune evasion by hexokinase2-mediated phosphorylation of IκBα, Cell Metab. 34 (2022) 1312–1324.e1316.
[26] Q. Zhu, H. Wang, S. Chai, L. Xu, B. Lin, W. Yi, L. Wu, O-GlcNAcylation promotes tumor immune evasion by inhibiting PD-L1 lysosomal degradation, PNAS 120 (2023) e2216796120.
[27] F. He, P. Zhang, J. Liu, R. Wang, R.J. Kaufman, B.C. Yaden, M. Karin, ATF4 suppresses hepatocarcinogenesis by inducing SLC7A11 (xCT) to block stress-related ferroptosis, J. Hepatol. 79 (2023) 362–377.
[28] Y. Yan, H. Teng, Q. Hang, L. Kondiparthi, G. Lei, A. Horbath, X. Liu, C. Mao, S. Wu, L. Zhuang, M. James You, M.V. Poyurovsky, L. Ma, K. Olszewski, B. Gan, SLC7A11 expression level dictates differential responses to oxidative stress in cancer cells, Nat. Commun. 14 (2023) 3673.
[29] J.L. Meitzler, H.R. Makhlouf, S. Antony, Y. Wu, D. Butcher, G. Jiang, A. Juhasz, J. Lu, I. Dahan, P. Jansen-Dürr, H. Pircher, A.M. Shah, K. Roy, J.H. Doroshow, Decoding NADPH oxidase 4 expression in human tumors, Redox Biol. 13 (2017) 182–195.
[30] Y. Xu, F. Fang, S. Miriyala, P.A. Crooks, T.D. Oberley, L. Chaiswing, T. Noel, A. K. Holley, Y. Zhao, K.K. Kiningham, D.K. Clair, W.H. Clair, KEAP1 is a redox sensitive target that arbitrates the opposing radiosensitive effects of parthenolide in normal and cancer cells, Cancer Res. 73 (2013) 4406–4417.
[31] J. Xu, C. He, Y. Cai, X. Wang, J. Yan, J. Zhang, F. Zhang, V. Urbonaviciute, Y. Cheng, S. Lu, R. Holmdahl, NCF4 regulates antigen presentation of cysteine peptides by intracellular oxidative response and restricts activation of autoreactive and arthritogenic T cells, Redox Biol. 72 (2024) 103132.
[32] A. Cheng, T. Xu, W. You, T. Wang, D. Zhang, H. Guo, H. Zhang, X. Pan, Y. Wang, L. Liu, K. Zhang, J. Shi, X. Yao, J. Guo, Z. Yang, A mitotic NADPH upsurge promotes chromosome segregation and tumour progression in aneuploid cancer cells, Nature Metabolism 5 (2023) 1141–1158.
[33] Y. Zhang, X. Du, Z. He, S. Gao, L. Ye, J. Ji, X. Yang, G. Zhai, A Vanadium-based nanoplatform synergizing ferroptotic-like therapy with glucose metabolism intervention for enhanced cancer cell death and antitumor immunity, ACS Nano 17 (2023) 11537–11556.
[34] T. Li, Y. Song, L. Wei, X. Song, R. Duan, Disulfidptosis: a novel cell death modality induced by actin cytoskeleton collapse and a promising target for cancer therapeutics, Cell Commun. Signal 22 (2024) 491.
[35] Y. Chen, B. Wu, H. Shang, Y. Sun, H. Tian, H. Yang, C. Wang, X. Wang, W. Cheng, Sono-immunotherapy mediated controllable composite nano fluorescent probes reprogram the immune microenvironment of hepatocellular carcinoma, Int. J. Nanomed. 18 (2023) 6059–6073.
[36] M.D. Wilkerson, D.N. Hayes, ConsensusClusterPlus: a class discovery tool with confidence assessments and item tracking, Bioinformatics (oxford, England) 26 (2010) 1572–1573.
[37] G. Yu, L.G. Wang, Y. Han, Q.Y. He, clusterProfiler: an R package for comparing biological themes among gene clusters, OMICS 16 (2012) 284–287.
[38] D. Zeng, Z. Ye, R. Shen, G. Yu, J. Wu, Y. Xiong, R. Zhou, W. Qiu, N. Huang, L. Sun, X. Li, J. Bin, Y. Liao, M. Shi, W. Liao, IOBR: Multi-omics immuno-oncology biological research to decode tumor microenvironment and signatures, Front. Immunol. 12 (2021) 687975.
[39] M.E. Ritchie, B. Phipson, D. Wu, Y. Hu, C.W. Law, W. Shi, G.K. Smyth, limma powers differential expression analyses for RNA-sequencing and microarray studies, Nucleic Acids Res. 43 (2015) e47.